Topics in Catalysis (2019) 62:977–988
https://doi.org/10.1007/s11244-019-01185-y

ORIGINAL PAPER

Gold Stabilized with Iridium on Ceria–Niobia Catalyst: Activity and Stability for CO Oxidation

Alejo Aguirre[1] · Rodolfo Zanella[2] · Celina Barrios[1] · Sandra Hernández[3] · Adrian Bonivardi[1,4] · Sebastián E. Collins[1,4]

Published online: 29 May 2019

Abstract
Monometallic gold and iridium, and bimetallic gold–iridium on ceria–niobia (Nb_2O_5–CeO_2) catalysts were synthesized by deposition–precipitation with urea. Ceria–niobia support, synthesized by co-precipitation, presented a higher reducibility and a higher surface acidity as a consequence of the deposition of niobia on the ceria surface. The Au–Ir/CeNb showed an enhanced activity and stability during the carbon monoxide oxidation reaction as compared with the monometallic catalysts. These catalysts were thoroughly characterized chemical and structurally. High-resolution electron microscopy, UV–Vis spectroscopy and CO adsorption showed evidences of iridium-gold closeness. In situ infrared spectroscopy in the diffuse reflectance (DRIFT) mode was used to investigate the reactivity of the active sites. A lower coverage of carbonate species was observed under reaction as a result of the presence of niobia in the catalyst formulation. Concentration-modulation excitation spectroscopy (c-MES) allowed a selective identification of intermediates and 'spectator' species. New adsorption sites for CO were identified and correlated with the high activity and stability of the bimetallic catalyst.

Keywords CO oxidation · Gold · Iridium · Ceria · DRIFT · Modulation excitation spectroscopy

1 Introduction

Gold-based catalysts supported on reducible oxides have been studied intensely because of their high activity towards oxidation reactions at low temperature [1–4]. Particularly CO oxidation [5–7], PROX (selective oxidation of CO in presence of an excess of H_2) [8, 9], low-temperature water gas shift [10], and total combustion of volatile organic compounds (VOC) [11–13] are among the most investigated reactions. It is well known that the catalytic activity on Au/oxide systems for CO oxidation strongly depends on the catalyst preparation method [14], the chosen supports [15], the catalyst pretreatment conditions [15], gold particle size [16], the effect of moisture on the catalytic reaction [17, 18] and metal/support interaction [19, 20]. One of the main issues regarding gold catalysts is their loss of activity during the reaction. In particular, decreased dispersion (sintering) of gold nanoparticles has been alleged as one of the major drawbacks. A key factor to improve the activity of gold catalysts is an appropriate choice of the support and the use of proper preparation and activation parameters during the synthesis methods. Many attempts have been made to stabilize gold catalysts by adding to them a second metal. Indeed, the anchoring of the gold particles by addition of a second metal, which decreases their surface mobility, is commonly presented as a viable alternative. Further, the addition of a second metal could change the electronic properties of gold particles, or it could change their local atom distribution by the formation of core–shell structures between gold and the added metal [21, 22]. Iridium has been used, showing

Electronic supplementary material The online version of this article (https://doi.org/10.1007/s11244-019-01185-y) contains supplementary material, which is available to authorized users.

✉ Sebastián E. Collins
scollins@santafe-conicet.gov.ar

[1] Instituto de Desarrollo Tecnológico Para La Industria Química (INTEC) - Universidad Nacional del Litoral and CONICET, Güemes 3450, 3000 Santa Fe, Argentina

[2] Instituto de Ciencias Aplicadas y Tecnología, Universidad Nacional Autónoma de México, Circuito Exterior S/N, Ciudad Universitaria, 04510 México City, Mexico

[3] Instituto de Industria (IDEI), Universidad Nacional de General Sarmiento (UNGS), Juan M. Gutiérrez 1150, B1613GSX Los Polvorines, Provincia de Buenos Aires, Argentina

[4] Facultad de Ingeniería Química, Universidad Nacional del Litoral, Santiago del Estero 2829, 3000 Santa Fe, Argentina

promising results in terms of stability and activity on titania [23–28] and on ceria [29].

The nature of the support on which gold is dispersed plays a crucial role in determining the catalytic activity for oxidation reactions. Moreover, there is an increase agreement in the literature that the oxidation reactions (e.g. CO oxidation) on gold/oxide catalysts proceed thought a metal-promoted Mars-Van Krevelen mechanism [30–32]. Among reducible oxides, cerium oxide has received special attention. Cerium oxide possess a remarkable oxygen storage capacity (OSC), which is linked to the creation, stabilization and diffusion of oxygen vacancies, especially in the oxide surface, due to the reversible redox property of the Ce^{4+}/Ce^{3+} pair. However, some authors have postulated that the deactivation of some of these cerium based systems can be attributed to the formation of strongly adsorbed carbonate species on ceria [15, 33–36]. The tuning of the surface acid-basic properties could be an appropriated strategy to improve the stability of these catalysts. Thus, promoting ceria with an acidic oxide such as niobium oxide, could modify acid–base properties and, at the same time, maintaining the redox properties of CeO_2 [37].

In this work a ceria–niobia supported gold–iridium catalyst was synthetized, characterized and evaluated in the CO oxidation reaction, as a prototypical reaction, in order to investigate the catalytic performance of these systems. In situ FTIR and UV–Vis spectroscopies in diffuse reflectance modes, under steady-state reaction conditions and in concentration-modulated experiments were employed to help understand the synergism between gold and iridium.

2 Experimental Section

2.1 Catalysts

Pure CeO_2 was obtained by inverse precipitation of an aqueous solution of $Ce(NO_3)_3{\cdot}6H_2O$ (99.99% Ce, Sigma-Aldrich), [0.24 M Ce], which was slowly added using a peristaltic pump (4 mL/min) to an aqueous solution of NH_4OH (25% wt/v, Merck). During the addition of the cation, the solution was vigorously stirred and the pH was kept at 8.5 by adding NH_4OH 12% wt/v to the suspension. The Ce-Nb oxide was prepared by co-precipitation using the same procedure. In this case, a mixed solution of 0.24 M of cerium nitrate and 0.17 M of oxalate ammonium niobiate [$NH_4NbO(C_2O_4)_2{\cdot}xH_2O$, 99.99% Nb Sigma-Aldrich] was added to the ammonium solution to obtain a solid with a nominal molar ratio $CeO_2/Nb_2O_5 = 95/5$. Each solid was centrifuged and washed five times with deionized water (ratio = 15 mL water/g dried support), dried overnight at 120 °C, and finally calcined in air at 450 °C. Hereafter, ceria–niobia support is named as CeNb.

Monometallic gold and iridium, and bimetallic gold–iridium, supported on CeNb catalysts were prepared by deposition–precipitation with urea (DPU) [29] using $HAuCl_4{\cdot}3H_2O$ (Sigma) and $IrCl_4{\cdot}H_2O$ (Sigma) as metal precursors. For the monometallic catalysts (Au or Ir nominal loading, 2 wt% each), 1 g of support was dispersed in an aqueous solution (50 mL) containing the metallic precursor (4.2×10^{-3} M) and urea (0.42 M). The suspension was heated to 80 °C for 16 h, under vigorous stirring and in the absence of light. Afterwards, the suspension was centrifuged to separate the solid phase, which was then washed with water and re-suspended. The new suspension was also centrifuged, and this procedure was repeated four more times. The recovered solid was dried in vacuum at 80 °C for 2 h.

The bimetallic Au–Ir/CeNb catalyst (nominal metals loading: 2 wt% ea.) was prepared by the sequential deposition method reported previously for a rutile catalyst, as follows [22]. Iridium was first deposited on ceria by the DPU method described above. The material was then dried at 80 °C and calcined in air (1 mL/min/mg) at 400 °C for 2 h, with a heating rate of 2 °C/min. Then, gold was deposited by the DPU method on the iridium-containing sample, in the dark. After gold deposition, the catalyst precursor was washed, and dried at 80 °C for 2 h.

All the catalysts were stored at room temperature under vacuum and in the darkness to prevent any alteration. Prior to use, the catalysts were activated in H_2 (1 mL/min/mg) at 400 °C for 2 h. A gold-supported on pure cerium oxide is used as reference material. This catalyst was previously characterized [29].

2.2 Characterization

Surface area (S_{BET}) of the support and catalyst was determined by nitrogen adsorption at 77 K using a Micromeritics ASAP 2020 instrument. X-ray powder diffraction patterns of the supports and reduced catalysts were measured at room temperature with a Shimadzu XD-D1 diffractometer using Cu Kα radiation.

Ultimate oxygen storage (OSC) capacity measurements were conducted by thermogravimetric analysis with a TA thermosbalance, model Q-600. 100 mg of sample was submitted to the following cleaning pretreatment: (i) reduction under H_2 flow up to 450 °C (10 °C/min) for 15 min, (ii) purge under pure He flow at 450 °C (15 min), (iii) oxidation under O_2 flow at 450 °C (15 min), (iv) cooling under O_2 flow from 450 to 200 °C, and (v) purge under He flow at 200 °C (15 min). After the cleaning pretreatment, a flow of 5% H_2/Ar was admitted at 200 °C and the temperature was increased by steps of 100 °C (1 h each), with a heating rate equal to 10 °C/min. All gas flows were set to 60 mL/min.

CO_2 adsorption was investigated at room temperature by in situ transmission Fourier transform infrared (FTIR)

spectroscopy. Self-supported wafers (30 mg) of the oxide samples were prepared by pressing at 5 ton cm^{-2} (wafer diameter = 13 mm). The sample disks were placed into a Pyrex IR cell fitted with water-cooled NaCl windows, which was attached to a conventional high vacuum system (base pressure = 1×10^{-4} Torr), equipped with a manifold for gas flow operation. Before the adsorption of CO_2, the sample were cleaned as follows: (i) heating from 25 to 450 °C (10 °C/min) in a flow of pure H_2 (50 mL/min), (ii) evacuation at 450 °C during 15 min; (iii) Re-oxidation under flowing O_2 (50 mL/min) at 450 °C for 15 min, (iv) cooling to 125 °C still under oxygen flow, (v) evacuation at 125 °C during 25 min, and (vi) cooling to 25 °C under dynamic vacuum. This cleaning procedure was considered to be the best option to thoroughly remove the surface carbonates from these oxides. Adsorption isotherms were recorded at 25 °C by progressively increasing the CO_2 partial pressure up to 760 Torr.

Metal loading was quantified by inductively coupled plasma atomic emission spectroscopy (ICP-AES) Iris Intrepid Thermo Elemental on the reduced catalyst. High resolution transmission microscopy (HRTEM) analysis was performed using a JEOL JEM 2010-F (200 kV) equipped with a Z-contrast annular detector. For the analyses, the reduced catalyst samples were deposited on a copper grid, coated with a porous carbon film. Digital image processing was made using the DigitalMicrograph software, version 3.7.0, Gatan Inc. High angle annular dark field (HAADF) observations of the catalysts were performed using a JEM 2010 FasTem analytical microscope equipped with a Z-contrast annular detector.

2.3 Catalytic Activity

The catalytic activity for CO oxidation [$CO(1\%) + O_2(1\%)$/He] was evaluated using a continuous plug-flow fixed bed microreactor at atmospheric pressure. For each experiment, 50 mg of powdered catalyst (40/60 mesh) diluted with 100 mg of quartz (100/120 mesh) was placed into the microreactor. The total flow was 100 mL/min. The experimental protocols followed heating/cooling cycles. During the first step of the cycle, the catalyst sample was heated from 0 to 200 °C, at a heating rate of 2 °C/min; then it was kept for 30 min at 200 °C. Finally, the temperature was decreased to room temperature using the same cooling rate. This heating/cooling cycle was repeated twice.

The outlet gas stream was analyzed continuously with an Agilent Technologies 6890 N online gas chromatograph equipped with a FID detector, a methanizer and a HP Plot Q column.

2.4 In Situ UV–Vis Diffuse Reflectance Spectroscopy (DRS)

UV–Vis DRS spectra of the catalysts were obtained using a CARY5000 spectrophotometer equipped with a Praying Mantis and a high temperature reaction chamber (Harrick). In each experiment, approximately 50 mg of the dried sample was packed in the sample holder and pretreated in situ under hydrogen flow (50 mL/min and 2 °C/min) at 400 °C for 2 h (R400). The isothermal reaction of CO oxidation [$CO(1\%) + O_2(1\%)$/He, 100 mL/min] was studied between 35 °C and 200 °C (steps of 25 °C) on the catalysts. UV–Vis DRS spectra were collected at each temperature once a steady state was reached during the thermal treatment under H_2 and under CO oxidation reaction.

2.5 In Situ FTIR Diffuse Reflectance (DRIFT) Spectroscopy

Infrared spectroscopy in the diffuse reflectance mode (DRIFT) mode was used to investigate, in situ, the adsorption and dynamic oxidation of CO on the catalysts. The DRIFT cell (Harrick, modified) was mounted inside the sample compartment of the FTIR spectrometer (Thermo-Electron, Nicolet 8700 with a cryogenic MCT detector). The spectrometer bench was continuously purged with dried air (Parker Balston FTIR purge gas generator) to eliminate CO_2 and water vapor contributions to the spectra.

Time-resolved IR spectra were recorded in kinetic and rapid-scan modes at a resolution of 4 cm^{-1}. The background spectrum was collected without catalyst. The amount of catalyst used in the DRIFT cell was 50 mg, with a bed height of about 5–7 mm. The cell was connected to the feed gas cylinders through low-volume stainless-steel lines. Rapid exchange of the gas composition was performed by switching an electronically actuated flow-through valve (Vici-Valco Instruments), which prevents pressure drop during changes, synchronized with the FTIR spectrometer. The gas flows were set by mass flow controllers. Before CO adsorption and reaction, the catalyst samples were reduced in situ under pure H_2 at 400 °C (2 h), and then cooled down to 35 °C under He flow.

The isothermal reaction of CO oxidation [$CO(1\%) + O_2(1\%)$/He, 100 mL/min] was studied between 35 and 200 °C (steps of 50 °C) on the preactivated catalysts. DRIFT spectra were collected at each temperature once a steady state of the infrared signal was reached (ca. 20 min).

Concentration-modulation excitation spectroscopy (c-MES) DRIFT experiments were performed at 35 °C, using the same set up already described elsewhere [38]. After recording the background spectrum, a modulation experiment was started by varying the inlet gas composition from CO(1%)/He to O_2(1%)/He, while maintaining the

same mass flow, using the desired modulation frequency. After allowing at least five modulation periods to adjust the system to the external perturbation the recording of the spectra was started. Spectra were acquired every 3 s, during each c-MES period, using reactants exchange frequencies from 1.7 to 33 mHz. Phase sensitive detection (PSD) analysis of the spectra was performed according to the method developed by Baurecht and Fringeli [39]. More details on the technique can be found in Supplementary Information. For clarity purposes, when indicated, the bands due to the P and R branches of CO in the gas phase were carefully subtracted from the spectra.

3 Results and Discussion

3.1 Catalyst Characterization

The chemical composition and textural properties of supports and catalysts are summarized in Table 1. The Nb loading in the mixed oxide determined by IPC was 3.4 wt% and the surface area was 66 m^2/g. The surface area of the catalysts was not modified after the deposition of gold and/or iridium on the ceria–niobia support. The measured metal loadings were slightly lower that the nominal amount.

The powder XRD patterns for the investigated samples showed only the characteristic peaks of a cubic, fluorite-type, structure (JCPDS 34-0394), with a calculated lattice parameter (a) of 0.541 nm, that is, no signals from niobium oxide were detected (see Fig. S1 in Supplementary Information). Moreover in the CeNb mixed oxide the same lattice parameter was calculated (0.541 nm), that is no shift or broadening of the peak corresponding to the plane (111) of the ceria was detected, which indicates the Nb^{5+} cations were not incorporated into the fluorite structure. TEM results indicate that niobia is equivalently distributed into the ceria (see below).

The presence of niobium oxide in the surface of the CeO_2, was investigated by CO_2 chemisorption. Since Nb_2O_5 is an acidic oxide, it is not able to adsorb CO_2 to form carbonate and bicarbonate surface groups. Figure 1 shows the integrated absorbance in the carbonate region, normalized by weight of the wafer and surface area, obtained at increasing CO_2 pressure into the IR cell at 25 °C. Clearly, the presence of niobia decreased the amount of basic surface sites able to form (bi)carbonate species. Additionally, ultimate oxygen storage capacity (OSC) of the synthesized oxides was measured to obtain quantitative information about the redox properties of CeNb compared with pure CeO_2. Figure 2 shows the results of OSC as the evolution of the amount of released oxygen per mass of CeO_2 with the increase of the temperature. Note that it is assumed that only the Ce^{4+} is reduced to Ce^{3+}, that is, considering that Nb^{5+} is not reduced, as was corroborated by X-ray photoelectron spectroscopy. The

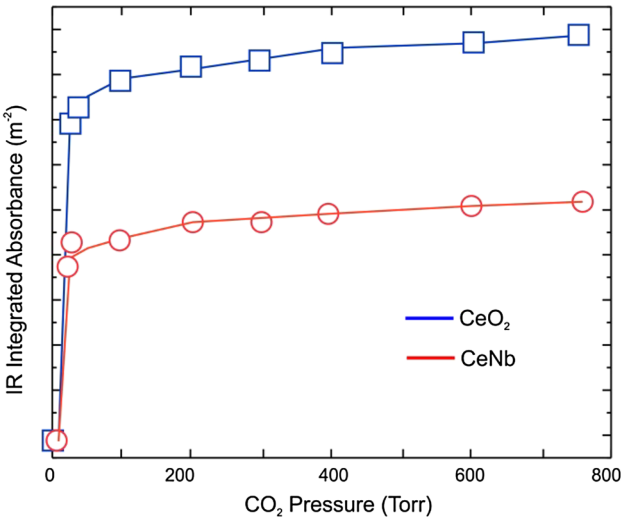

Fig. 1 Integrated area of the infrared signals in the carbonate region for CeO_2 and CeNb supports

Table 1 Main characteristics of the catalyst and supports and T_{50} values for CO oxidation

Catalyst	Nb (wt%)[a]	Metal loading[a] (wt%)		S_{BET} (m^2/g)	Average particle size (nm)[b]	T_{50} CO oxidation (°C)[c]			
		Au	Ir			Heating 1	Cooling 1	Heating 2	Cooling 2
Ir/CeNb	3.40	–	2.1	63	2.5	90	198	210	227
Au/CeNb	3.40	1.9	–	61	3.1	84	8	12	11
Au–Ir/CeNb	3.40	1.7	2.1	62	3.5	80	< 20	< 20	< 20
CeNb	3.40	–	–	62	–	310	–	–	–
Au/CeO_2	–	1.8	–	66	2.1	22	20	22	58
CeO_2	–	–	–	67	–	–	–	–	–

[a]Determined by ICP

[b]Determined by TEM

[c]T_{50} reported for the cooling cycles are indicative due to fluctuations in the temperature during the cooling of the reactor

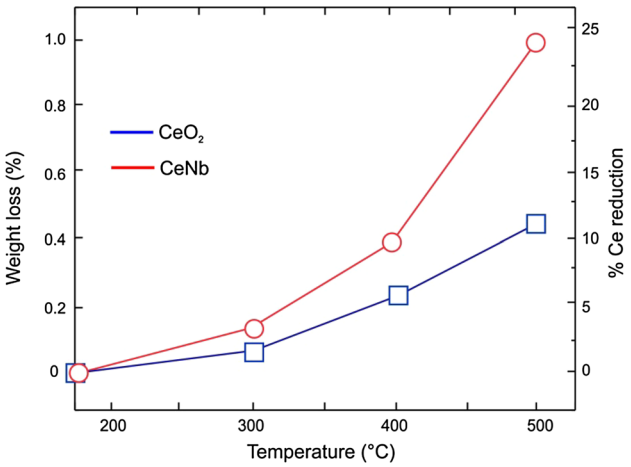

Fig. 2 Oxygen storage capacity (OSC) versus the temperature of reduction for pure CeO_2 and cerium-niobium mixed oxide (CeNb)

reducibility of pure ceria increases from 1.6 to ca. 10% when reduced from 300 to 500 °C. However, in the mixed oxide, the percentage of Ce^{4+} reduction goes from 4 to almost 25% when reduced from 300 to 500 °C. This result indicates a clear promotion of the ceria reduction by the presence of surface niobia species.

Regarding the increase of the reducibility of ceria by the interaction with niobia, similar results were reported by Ramírez-Cabrera et al. [40] and Stosic et al. [41]. It is therefore likely that the oxide–oxide interface (Nb_2O_5–CeO_2) would be a critical factor for enhanced reduction of Ce^{4+} to Ce^{3+}, as experimentally and theoretically demonstrated in the case of the analogous system V_2O_5–CeO_2 [42–45].

3.2 Catalytic Activity

In order to assess their activity and stability, two consecutive heating and cooling reaction cycles were performed. Figure 3 shows the light-off curves for the CO oxidation over the whole set of catalysts, and the temperatures for the 50% of CO conversion are summarized in Table 1.

The CeNb support was only active above 150 °C. The Ir/CeNb catalyst showed a rather low initial activity to oxidize CO reaching almost 100% conversion at around 200 °C (Fig. 3a). Moreover, a noticeably decrease in activity occurred during the second reaction cycle, probably due to the oxidation of the iridium. The T_{50} increased from 190 °C during the first heating ramp to 210 and 225 °C in the cooling and second heating cycles. A similar behavior was reported before for Ir/CeO_2 and Ir/TiO_2 catalysts [23, 24, 29].

Figure 3b shows that the monometallic Au/CeO_2 catalyst presented a high initial activity, reaching a complete CO conversion at approximately 80 °C. The catalytic performance of this catalyst was similar to the one reported for other gold–ceria catalysts under similar reaction conditions [29, 32, 46]. A closer inspection of the evolution of the conversion during the reaction cycles shows that some deactivation took place, though (viz., T_{50} increased from 34 to 41 °C).

The behavior of the monometallic Au/CeNb catalyst is different from the previous one. In this case, the initial activity for CO oxidation is low and increases with temperature, reaching the complete conversion of CO at 120 °C (Fig. 3c). Noticeably, during the cooling step and during the next cycle the catalyst was more active, and remained stable as well. The activity towards CO oxidation remained high, with of T_{50} of only 10 °C.

Finally, a similar behavior was found for the Au–Ir/CeNb catalyst (Fig. 3d). Again, the first heating curve presented low activity, but the following ramps showed a high activity and a remarkable stability, that is, no indication of change in activity between the first cooling and the second heating and cooling cycle was observed.

Summarizing, for CO oxidation activity and stability on Au/CeNb and Au–Ir/CeNb is clearly improved with respect to either the monometallic iridium or pure ceria, once activated under reaction. This behavior suggests an active interaction between Au and Ir, as it is discussed below.

3.3 Catalyst Nanostructural Characterization

To evaluate the nanostructural characteristics of mono and bimetallic catalyst supported on CeNb, (S)TEM investigations were performed. Figures S2–S4 show representative HAADF-STEM and HRTEM images of the support, Au/CeNb and Au–Ir/CeNb catalysts. Chemical analysis by X-ray energy-dispersive spectroscopy (X-EDS) showed a homogeneous distribution of niobium on the support, with a loading in the range determined by ICP. It is important to notice that no segregated Nb_2O_5 crystals could be detected, in agreement with XRD results. HRTEM images of the same support allowed the analysis of the digital diffraction patterns (DDPs) in the selected areas showing nanocrystals with 3.1 Å [1 1 1]F, 2.7 Å [2 0 0]F and 1.9 Å [2 2 0]F spacings, which are typical of the fluorite-type structure of CeO_2. Au (1 1 1) planes were detected by DDPs of selected areas in the HRTEM images from its characteristic d-spacing of 0.23 nm. The supported nanoparticles are homogeneously distributed on the support, with average sizes: 2.5 nm for Ir and 3.1 nm for Au and 3.5 for Au–Ir (Table 1). The nanostructural and nanoanalytical analysis suggests a close interaction between gold and iridium. Some individual metal particles were selected for chemical analysis by X-EDS as showed in Figure S4(D). Results indicated that gold and iridium are present in the same region. Akita et al. [27] nicely showed the close interaction between gold and iridium in a titania-supported catalyst. A careful high-resolution TEM

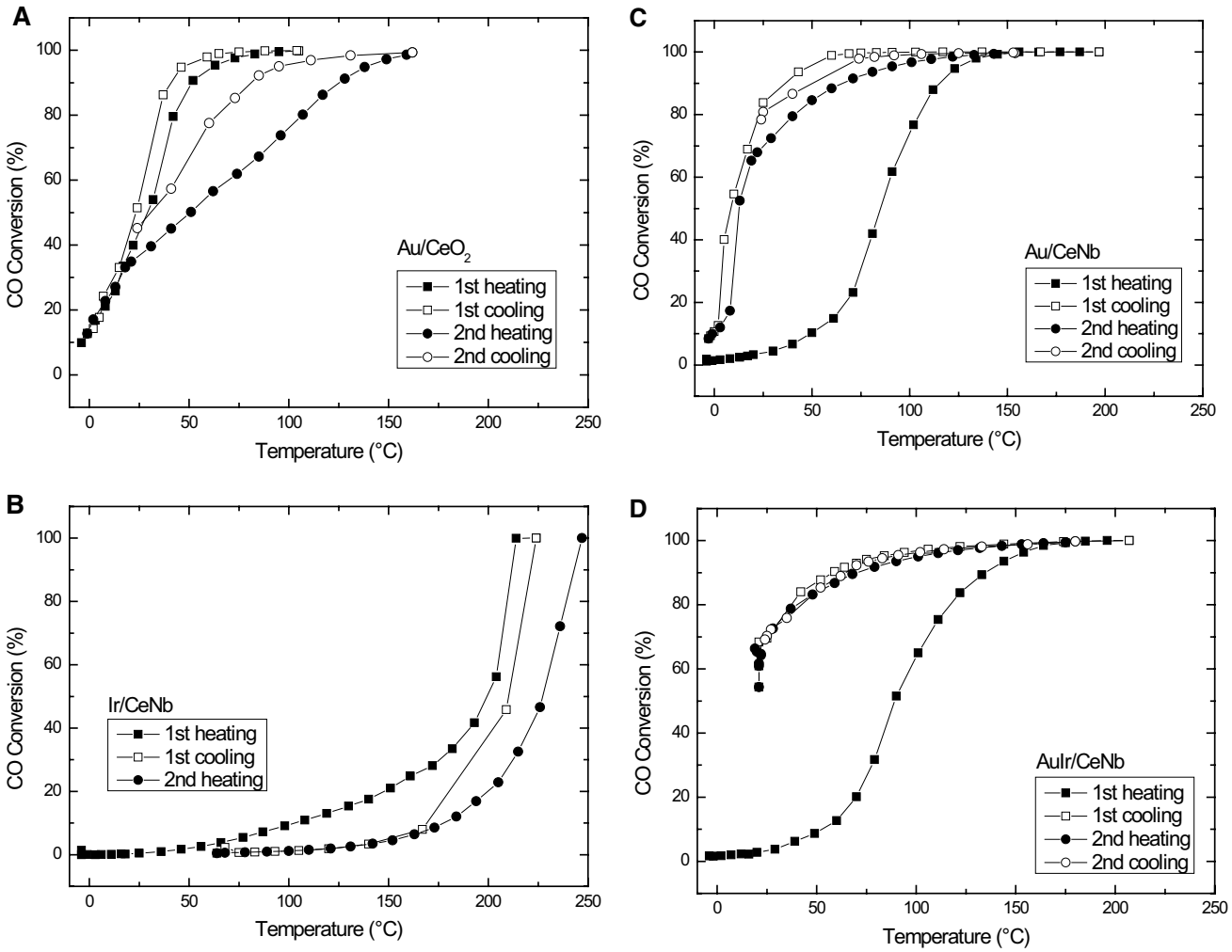

Fig. 3 Evolution of the CO conversion on the Au/CeO2 (**a**), Ir/CeNb (**b**), Au/CeNb (**c**) and Au–Ir/CeNb (**d**) catalysts during consecutive heating and cooling cycles. Reaction conditions: CO(1%) + O_2(1%)/He, total flow: 100 mL/min, 50 mg of catalyst

investigation, allowed them to observe an epitaxial contact between the Au nanoparticle/IrO_2 pillar. Similar conclusions were achieved by Han et al. [47]. Our TEM results, from a highly porous and dense oxide as ceria, did not allow observing the formation of an alloy or bimetallic particles. Digital diffraction patterns (DDPs) in the selected areas do not show conclusive results since the spacing are in the same range that monometallic gold.

3.4 In Situ UV–Vis DRS

To further characterize the interaction of the Au–Ir, in situ DRS studies were performed. UV–Vis spectra were recorded during the in situ activation under hydrogen at increasing temperature between room temperature and 400 °C (Fig. 4). For the monometallic Ir/CeNb sample (Fig. 4a), there is an absorbance increase in the visible region that can be associated with the change of the sample color, indicating the reduction of iridium during the treatment. In the case of the Au/CeNb catalyst, Fig. 4b shows the development of a broad band centered at 540 nm that rises in intensity as the reduction temperature increases. This band at 535 nm is associated with the surface plasmon resonance (SPR) of metallic gold [48]. For the bimetallic AuIr/CeNb sample (Fig. 4c), the plasmon band of Au^0 is observed shifted to 525 nm and with a lower intensity compared with the monometallic gold.

Figure 5 compares the DRS spectra under CO oxidation reaction after the catalyst activation (R400) and first heating–cooling cycle. As seen in the spectra, the plasmon shape and intensity is maintained in the Au/CeNb and Au–Ir/CeNb catalysts. When compared, the plasmon band in the Au–Ir is shifted and less intense than in the mono metallic one. The plasmon band shape, position and intensity depend on the particle size, shape and surrounding environment. Since the metal particles in Au/CeNb and Au–Ir/CeNb samples have similar average size (Table 1), the shift and attenuation of

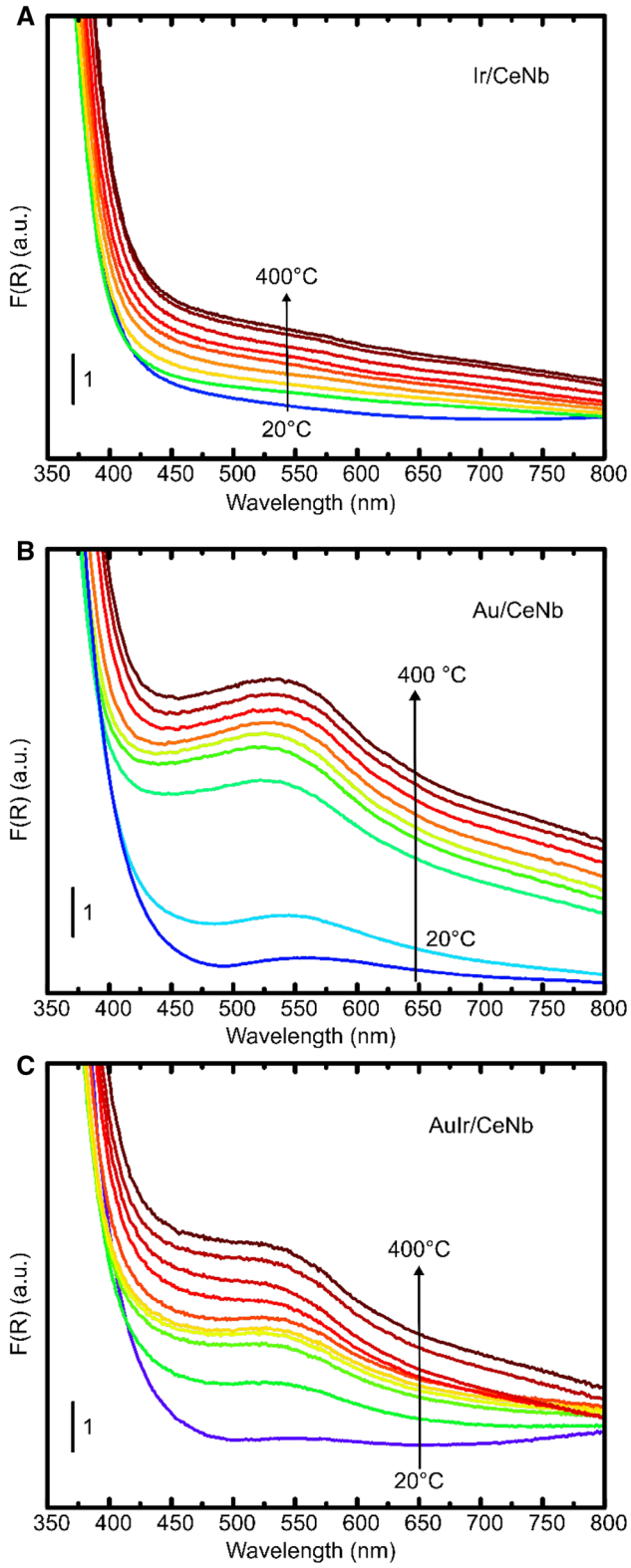

Fig. 4 Pre-treatment: from 20 to 400 °C, flowing pure H_2: **a** Ir/CeNb, **b** Au/CeNb, **c** AuIr/CeNb

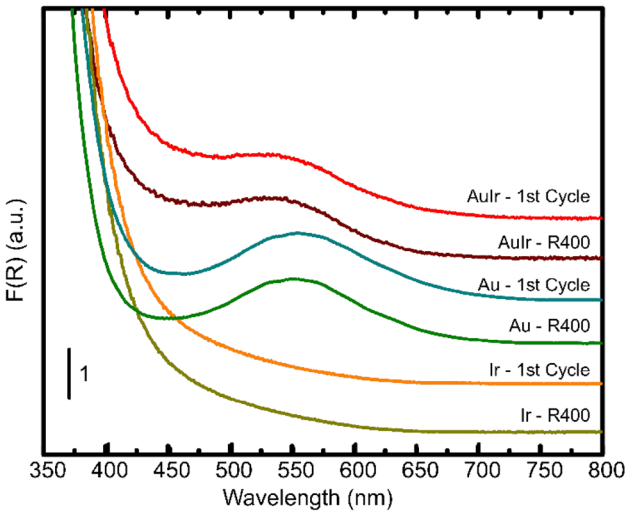

Fig. 5 DRS UV–Vis spectra collected under flow of CO(1%)/He at 25 °C on the catalysts after activation of the catalyst under pure H_2 at 400 °C (R400); and after the first CO oxidation cycle heating and cooling from 25 to 200 °C (1st Cycle)

the SPR band in the bimetallic system indicates an interaction of Ir with Au in the particles.

3.5 In Situ DRIFT Spectroscopy

3.5.1 CO Adsorption

With the aim of understanding the origin of the variations observed in the catalytic performance a series of DRIFT studies were conducted. Figures 6, 7 and 8 show DRIFT spectra after CO adsorption at 25 °C on the catalyst after activation (R400) and after each reaction cycles carried out on the DRIFT cell. The spectra were recorded under steady state conditions during CO(1%)/He flow and were deconvoluted after careful substraction of gaseous CO(g) signal.

Au/CeNb catalyst shows a band at 2130 cm^{-1}—already presented before the CO adsorption—due to the forbidden electronic transition $^2F_{5/2} \rightarrow {}^2F_{7/2}$ of Ce^{3+} [49, 50]. This band is generated during the reduction pre-treatment and was observed in all the activated catalysts. The characteristic bands due to CO adsorbed on gold sites (Fig. 6) are assigned as follows: a signal at 2107 cm^{-1} corresponding to Au^0–CO [51–54]; and bands below 2100 cm^{-1} to CO chemisorbed on negatively charged gold species, $Au^{\delta-}$ [55, 56]. The red-shift of these bands with respect to that of CO adsorbed on zero valent gold has been attributed to the back-donation of charge from partial negatively charged Au species to the 2π* antibonding orbital of CO [57–59]. After the reaction cycles, the Ce^{3+} signal disappeared as a consequence of the oxidative atmosphere, and changes in the CO-gold sites features are also observed. Mainly, the signal due to

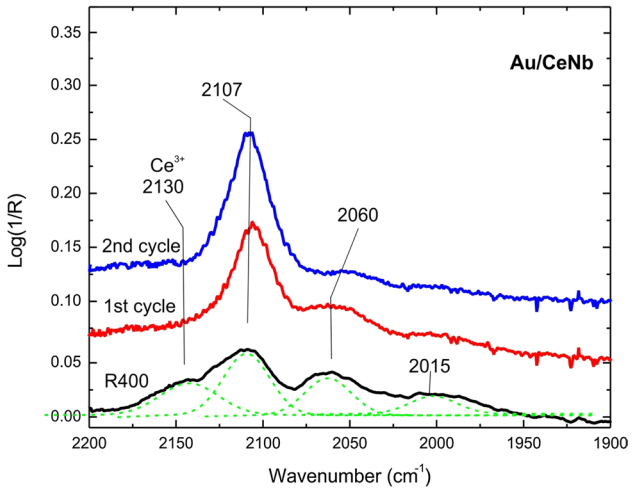

Fig. 6 DRIFT spectra collected under flow of CO(1%)/He at 25 °C on the Au/CeNb catalyst after: (i) activation of the catalyst under pure H_2 at 400 °C, (ii) the first CO oxidation cycle heating and cooling from 25 to 200 °C, and (iii) the second CO oxidation cycle from 25 to 200 °C

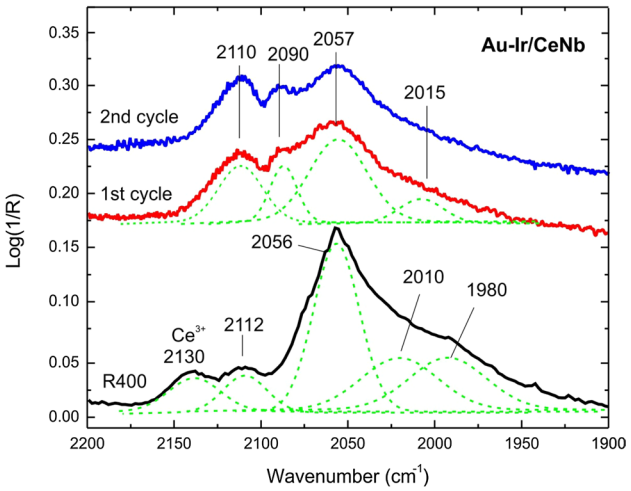

Fig. 8 DRIFT spectra collected under flow of CO(1%)/He at 25 °C on the Au–Ir/CeNb catalyst after: (i) activation of the catalyst under pure H_2 at 400 °C, (ii) the first CO oxidation cycle heating and cooling from 25 to 200 °C, and (iii) the second CO oxidation cycle from 25 to 200 °C

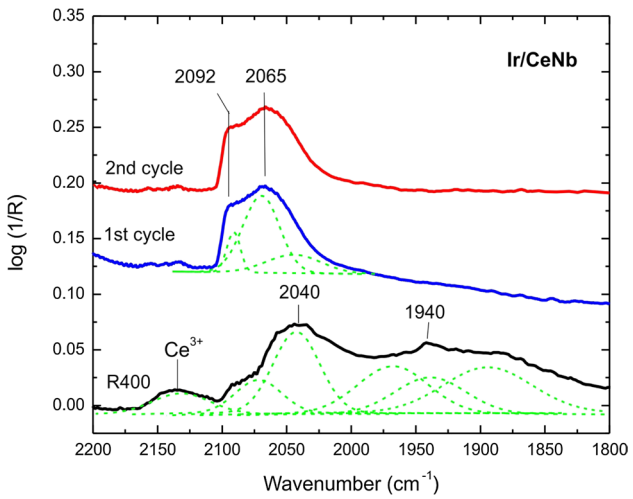

Fig. 7 DRIFT spectra collected under flow of CO(1%)/He at 25 °C on the Ir/CeNb catalyst after: (i) activation of the catalyst under pure H_2 at 400 °C, (ii) the first CO oxidation cycle heating and cooling from 25 to 200 °C, and (iii) the second CO oxidation cycle from 25 to 200 °C

Au^0–CO increases in the first cycle and slightly increases in the second reaction cycle. Signals below 2100 cm^{-1} also decreased their intensity. This last decrease could be due to some loss of the metal dispersion. A similar behaviour was registered in the reference Au/CeO_2 catalyst reduced at 400 °C, a sharp and intense absorption band at 2105 cm^{-1} was observed and assigned to CO adsorbed on neutral gold (Au^0). Additionally, a small feature at 2060 cm^{-1} is usually attributed to CO chemisorbed on partially negatively charged gold sites ($Au^{\delta-}$).

After adsorption of CO on the reduced Ir/CeNb catalyst, the IR spectrum exhibited a complex features (Fig. 7). As mentioned before, the signal of Ce^{3+} is observed after the reduction at 400 °C, but it is lost after the CO oxidation reaction cycles. In the carbonyl region, a signal centered at 2040 cm^{-1} and a broad band in the 2000–1800 cm^{-1} range are registered. Studies of carbon monoxide adsorption on iridium metal single crystals and supported iridium catalyst assigned an infrared peak in the range 2100–2000 cm^{-1} to linear CO species (on-top site) [60–64]. Additional broad bands in the range of 2000–1800 cm^{-1} were ascribed to bridged CO on iridium metal films and iridium cluster carbonyl complex [65] and in iridium organometallic compounds [66, 67]. Thus, the signals in the 2100–2000 cm^{-1} region are assigned to linearly adsorbed CO and the broad band below 2000 cm^{-1} to bridged CO on Ir^0 sites, as expected due to the strong reduction pre-treatment. After the two consecutive CO oxidation reaction cycles up to 200 °C, only a main feature remains in the spectra, composed by two overlapped peaks at 2094 and 2068 cm^{-1}. A set of two bands at 2107–2050 cm^{-1} have been attributed to the symmetric and antisymmetric modes of $Ir^+(CO)_2$ dicarbonyl species and polycarbonyls, e.g., $Ir^+(CO)_3$ species [68]. Then, it is likely that after the oxidation cycles, the small iridium particles were partially oxidized, which is in agreement with the progressive loss of catalytic activity (Fig. 3b). After the consecutive reaction cycles, the main features in the infrared spectra do not change, but a slight increase

in the intensity of the infrared signals is register. Particularly, during the first cycle, an increase in the band at 2067 cm^{-1} is observed, which decrease in the second cycle. This change in the infrared spectra could be related with the slight decrease in the catalytic activity registered during the light-off cycles (Fig. 3b).

The DRIFT spectra of adsorbed CO on the Au–Ir/CeNb bimetallic catalyst present some distinctive features, i.e. it is not a linear combination of the monometallic ones (Fig. 8). The characteristic feature due to Au^0–CO species appeared at 2112 cm^{-1}. Additional peaks at 2056, 2010 and 1980 cm^{-1} are observed. The low frequency band at 1980 cm^{-1} can be related to reduced iridium sites, however the precise assignation of the signals between 2100 and 2000 cm^{-1} is not straightforward. After the CO oxidation cycles, changes in the spectra are registered. Similar as before, Ce^{3+} signal disappeared and the band at 2110 cm^{-1} due to Au^0–CO gained intensity. The band at 2060 cm^{-1} lost intensity and a shoulder at 2096 cm^{-1} was observed [52]. The band at ca. 2010 cm^{-1} retained its intensity but the low frequency feature at 1980 cm^{-1} was lost. This last feature can be ascribed to metallic iridium sites, in analogy to the observed on Ir/CeNb. It is important to note that the infrared spectra did not change during the consecutive reaction cycles, in line with the CO oxidation stability observed on the Au–Ir/CeNb catalyst (Fig. 3d).

3.5.2 In Situ CO Oxidation in Steady-State

Additionally, two consecutive reaction cycles heating and cooling between 25 and 200 °C under CO(1%)/O_2(5%)/He flow were performed and monitored by in situ DRIFT, on the monometallic and bimetallic catalysts. Figure 9 shows steady state infrared spectra under reaction at 50 °C, after the second cycle. As shown in this last figure, signals due to CO adsorbed on metallic sites are present. The infrared signals due to CO adsorbed on iridium in the Ir/CeO_2 catalyst only showed small changes through the reaction cycle. The high heat of adsorption of CO on Ir sites ($E_0 = 225$ kJ/mol and $E_1 = 115$ kJ/mol) is consistent with the high coverage observed up to 200 °C, the maximum temperature used in this work [69]. Conversely, the signals due to CO adsorbed on gold sites lost intensity upon heating, which is expected [55]. But the most remarkable feature is the difference in the carbonate region between the Au/CeO_2 catalyst and the metallic catalysts supported on cerium-niobia. As shown before a strong suppression of the (bi)carbonates surface species is observed, which is the result of the increased surface acidity provided by Nb_2O_5 on the niobium-containing ceria support (see Fig. 1).

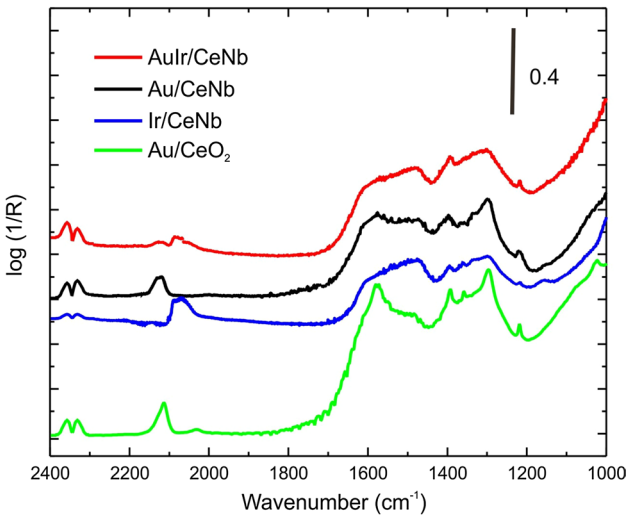

Fig. 9 In situ infrared spectra collected under reaction at 50 °C, after completing two consecutive reaction cycles. Reaction condition: CO(1%)/O_2(5/ %)/He, 50 mL/min. Spectra were collected at a resolution of 1 cm^{-1} and CO gas signals are substrated

3.5.3 In Situ c-MES CO Oxidation

It is clear that kinetically relevant information on the reactivity of the adsorbed species from spectra collected under steady state, even employing different temperatures, is difficult to obtain. Particularly, it is almost impossible to distinguish intermediates from spectators. Therefore, concentration-modulation excitation spectroscopy (c-MES) experiments were performed to investigate the dynamics of the reactivity of the CO adsorbed species. Spectra were further analyzed by carrying out a phase sensitive detection (PSD) treatment of the data (see Supplementary Information for further details). Figures 10 and 11 show the time-domain spectra during a complete period, 60 s, exchanging from CO(1%)/He to O_2(1%)/He on the stabilized catalysts at 50 °C, and the phase-domain spectra, respectively. As previously shown, the catalytic activity of the monometallic iridium catalyst at this temperature was very low and; therefore, no change in the CO bands was observed (spectra presented in Fig. S5).

Figure 10 shows the time-domain and phase-domain spectra for the monometallic Au/CeNb catalyst during the c-MES experiment. The signal from adsorbed CO on metallic gold sites (2110 cm^{-1}) was clearly affected by the periodic exchange of reactants. Notably, the band at 2060 cm^{-1} assigned to $Au^{\delta-}$–CO species is very weak under reaction mixture. The production of CO_2 (2350 cm^{-1}) in the gas phase was observed in-phase with the CO adsorbed species. This clearly shows that CO on gold sites are the active species in the oxidation of CO on this catalyst, as previously reported for other supported gold materials [53, 54, 70–72].

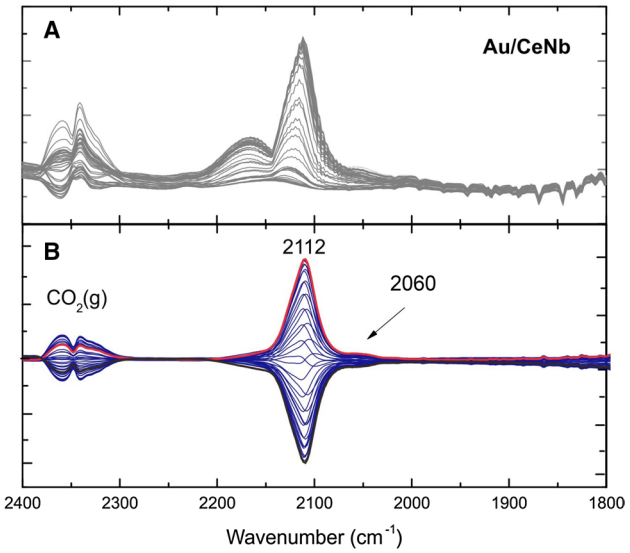

Fig. 10 **a** Time-domain DRIFT spectra during a c-MES cycle of $CO(1\%)+O_2(1\%)$/He switched to He over Au–Ir/CeNb (50 mL/min, 50 °C, ω = 8.33 mHz); **b** phase-domain spectra after PSD demodulation. Gas phase signals from CO were carefully subtracted in (**b**)

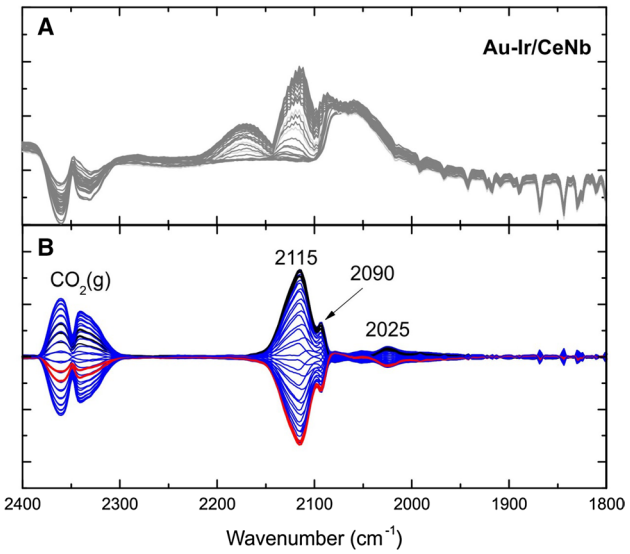

Fig. 11 **a** Time-domain DRIFT spectra during a c-MES cycle of $CO(1\%)+O_2(1\%)$/He switched to He over Au–Ir/CeNb (50 mL/min, 50 °C, ω = 8.33 mHz); **b** phase-domain spectra after PSD demodulation

Goodman et al. showed that gold films (mono- and bilayer structures) grown on reduced TiO_2 exhibited very high activity in CO oxidation [55, 56]. This observation allowed them to conclude that negatively charged gold species play a major role in the reaction. Similar conclusions were drawn from studies carried out on powdered MgO- and CeO_2-supported gold particles catalysts [57, 58].

For the bimetallic Au–Ir/CeNb, the most active and stable catalyst, infrared results are more complex to interpret (Fig. 11). The time-domain spectra present a combination of bands, as shown before in Fig. 8, most of which remained constant upon switching the reactants. However, after a PSD analysis, the phase-domain spectra in Fig. 11b allow discerning which signals were affected by the perturbation (note again that for clarity the CO gas bands were subtracted from the spectra). In this case, it can be appreciated that the signals assigned to Ir sites at ca. 2060–2010 cm^{-1} remain constant. Then, it can be concluded that Ir–CO species are not oxidized at 50 °C and are mere spectators of the reaction at this temperature, as in the case of Ir/CeNb. This last observation supports the previous assignment of this band (Fig. 8). Conversely, as in the monometallic gold system, the Au^0–CO species (at 2110 cm^{-1}) clearly participates in the reaction. Additionally, new bands are observed to change at 2090 cm^{-1} and at 2025 cm^{-1}, which are synchronous with the production of CO_2. The position and shape of these bands were different from those registered on the monometallic gold catalyst under reaction. Then, these signals might be tentatively assigned to low-coordination and/or negatively charged gold sites or surface isolated gold sites (by iridium atoms), in a cluster or nanoparticle. This, could be due to an electronic perturbation/change of the gold sites as a consequence of the contact with iridium. The presence and persistence of these new reactive sites in the Au–Ir bimetallic catalyst is correlated with the high activity and stability of the bimetallic Au–Ir/CeNb catalyst.

In a recent work, by means of in situ time-resolved DRIFT spectroscopy, some of us observed, that CO species on gold sites with IR bands below 2100 cm^{-1} (assigned to CO adsorbed on negatively charged gold clusters, $Au^{\delta-}$) are the most reactive intermediates for the CO oxidation on a well-characterized $Au/CeZrO_2$ catalyst [70]. Moreover, the inhibitory role of CO_2 in the inhibition of the mechanism of CO oxidation was thoroughly investigated by means of isotopic transient analysis ($^{13}CO/^{12}CO_2$) monitored by mass spectrometry and by time-resolved DRIFT spectroscopy [70]. It was shown that a competitive adsorption of CO_2 on reactive surface O sites at the metal-support interphase, producing adsorbed carbonate species, can partially hinder the replenishment of the vacancies by molecular oxygen. This model was validated by simulating the microkinetic mechanism and fitting the temporal evolution of the IR signals of CO adsorbed species. On this basis, we can conclude that the higher activity and stability of the Au–Ir/CeNb catalyst, as compared with the reference Au/CeO_2, is the result of the generation of new metal sites in the Au–Ir particles, where CO can be adsorbed and react, and of the inhibition of the formation of surface carbonate species due to the presence of acidic niobia, which enhances the redox capacity of the ceria.

4 Conclusions

A CeO_2–Nb_2O_5 (CeNb) mixed oxide support was synthetized by a co-precipitation method. Chemical and structural characterization showed that niobia was not incorporated in the ceria structure, but was highly disperse in the same. The CeNb material has lower surface basicity, as revealed by CO_2 adsorption, and an enhanced reducibility as compared to pure ceria. Gold, iridium and bimetallic gold–iridium catalysts were synthesized by the deposition–precipitation method with urea over the mixed ceria–niobia support. In comparison with the monometallic gold or iridium catalysts, the bimetallic Au–Ir/CeNb catalyst exhibited noticeable activity improvement for CO oxidation, together with superior stability. The origin of the observed synergy was investigated by combining different characterization techniques. HRTEM images with nanoanalysis by X-EDS, in situ UV–Vis DRS and CO adsorption monitored by in situ DRIFT spectroscopy revealed an Au–Ir on the supported-CeNb catalyst.

In situ CO oxidation experiments under steady state conditions showed a lower amount of spectator carbonate species on the CeNb supported catalysts as compared with the reference Au/CeO_2. In situ c-MES DRIFT experiments were used to obtain dynamic information about the reactivity of chemisorbed CO species. It was shown that Ir-CO species are not reactive at 50 °C, but Au^0–CO species are active in the mono- and bimetallic gold catalyst. Additionally, new active sites ($Au^{\delta-}$) are produced when gold and iridium coexist, which increases catalytic activity.

The results presented here for Au–Ir/CeNb prove that the combination of a niobia-modified ceria support, which has a higher reducibility and a more acidic surface, together with the appearance of new metal catalytic sites as consequence of the intimacy between gold and iridum, was able to produce a highly active and stable catalytic system. We believe that the present work could be valuable for strategies with the aim of designing more active and stable gold catalyst by employing a second metal to produce isolated reactive gold sites and a modified support to improve its reducibility and acidity.

Acknowledgements The authors acknowledge the financial support from ANPCyT PICT-2014-0497, PIP-CONICET-2015-086CO, ASECTEI-Santa Fe 2010-067-13, and the bi-national project CONICET—CONACYT (2013), PAPIIT 103719 and CONACYT A1-S-18269 Grants. We thank V. Maturano-Rojas and Selene Islas for technical assistance.

References

1. Hutchings GJ, Brust M, Schmidbaur H (2008) Chem Soc Rev 37:1759–1765
2. Haruta M, Yamada N, Kobayashi T, Iijima S (1989) J Catal 115:301–309
3. Haruta M, Kobayashi T, Sano H, Yamada N (1987) Chem Lett 16:405–408
4. Bond GC, Louis C, Thompson DT (2006) Catalysis by gold. Imperial College Press, London
5. Dobrosz-Gómez I, Kocemba I, Rynkowski J (2009) Catal Lett 128:297
6. del Río E, Blanco G, Collins SE, Haro M, Chen X, Delgado J, Calvino J, Bernal S (2011) Top Catal 54:931
7. Laguna OH, Romero Sarria F, Centeno MA, Odriozola JA (2010) J Catal 276:360
8. Cargnello M, Gentilini C, Montini T, Fonda E, Mehraeen S, Chi M, Herrera-Collado M, Browning ND, Polizzi S, Pasquato L, Fornasiero P (2010) Chem Mater 22:4335
9. Tibiletti D, Fonseca A, Burch R, Chen Y, Fisher J, Goguet A, Hardacre C, Hu P, Thompsett D (2005) J Phys Chem B 109:22553
10. Pilasombat R, Daly H, Goguet A, Breen J, Burch R, Hardacre C, Thompsett D (2012) Catal Today 180:131
11. Scire S, Liotta L (2012) Appl Catal B 125:222
12. Scire S, Riccobene P, Crisafulli C (2010) Appl Catal B 101:109
13. Delannoy L, Fajerwerg K, Lakshmanan P, Potvin C, Méthivier C, Louis C (2010) Appl Catal B 94:117
14. Haruta H (1997) Catal Surv Asia 1:61–73
15. Collins SE, Cies JM, del Rio E, Lopez-Haro M, Trasobares S, Calvino JJ, Pintado JM, Bernal S (2007) J Phys Chem C 111:14371–14379
16. Haruta M (1997) Catal Today 36:153–166
17. Daté M, Okumura M, Tsubota S, Haruta M (2004) Angew Chem 116:2181–2184
18. Olmos CM, Chinchilla LE, Delgado JJ, Hungría AB, Blanco G, Calvino JJ, Chen X (2016) Catal Lett 146:144–156
19. Ta N, Liu J, Chenna S, Crozier PA, Li Y, Chen A, Shen W (2012) J Am Chem Soc 134:20585–20588
20. Lin Y, Wu Z, Wen J, Ding K, Yang X, Poeppelmeier KR, Marks LD (2015) Nano Lett 15:5375–5381
21. Hosseini M, Siffert S, Tidahy HL, Cousin R, Lamonier J-F, Aboukais A, Vantomme A, Roussel M, Su B-L (2007) Catal Today 122:391–396
22. Calzada LA, Collins SE, Han CW, Ortalan V, Zanella R (2017) Appl Catal B 207:79
23. Petrova P, Tabakova T, Munteanu G, Zanella R, Tsvetkov M, Ilieva L (2013) Catal Commun 36:84
24. Bokhimi X, Zanella R, Angeles-Chávez C (2010) J Phys Chem C 114:14101
25. Gomez-Cortés A, Díaz G, Zanella R, Ramírez H, Santiago P, Saniger J (2009) J Phys Chem C 113:9710
26. Okumura M, Akita T, Haruta M, Wang X, Kajikawa O, Okada O (2003) Appl Catal B 41:43
27. Akita T, Okumura M, Tanaka K, Tsubota S, Haruta M (2003) J Electron Microsc 52(2):119
28. Zhao J, Jun NI, Xu J, Xu J, Cen J, Li X (2014) Catal Commun 54:72
29. Aguirre A, Barrios CE, Aguilar-Tapia A, Zanella A, Baltanas MA, Collins SE (2016) Top Catal 59:347
30. Lohrenscheit M, Hess C (2016) ChemCatChem 8:523–526
31. Schlexer P, Widmann D, Behm J, Pacchioni G (2018) ACS Catal. 8(7):6513–6525
32. Widmann D, Behm RJ (2014) Acc Chem Res 47(3):740–749
33. Deng W, Flytzani-Stephanopoulos M (2006) Angew Chem Int Ed 118:2343–2347
34. Deng W, Flytzani-Stephanopoulos M (2006) Angew Chem Int Ed 45:2285
35. Karpenko A, Denkwitz Y, Plzak V, Cai J, Leppelt R, Schumacher B, Behm RJ (2007) Catal Lett 116:105–115
36. Abd El-Moemen A, Karpenko A, Denkwitz Y, Behm RJ (2009) J Power Sources 190:64–75

37. Jardima EO, Rico-Francésa S, Coloma F, Anderson JA, Ramos-Fernandeza E, Silvestre-Albero J, Sepúlveda-Escribano A (2015) Appl Catal A 492:201–211
38. Aguirre A, Collins SE (2013) Catal Today 205:34–40
39. Baurecht D, Fringeli UP (2001) Rev Sci Inst 72:3782–3792
40. Ramírez-Cabrera E, Atkinson A, Chadwick D (2002) Appl Catal B 36:193
41. Stosic D, Bennici S, Rakic V, Auroux A (2012) Catal Today 192:160
42. Martínez-Huerta MV, Deo G, García-Fierro JL, Bañares MA (2007) J Phys Chem C 111:18708
43. Martínez-Huerta MV, Coronado JM, Fernández-García M, Iglesias-Juez A, Deo G, García-Fierro JL, Bañares MA (2004) J Catal 225:240
44. Popa C, Ganduglia-Pirovano M, Sauer J (2011) J Phys Chem C 115(15):7399–7410
45. Wu X-P, Gong X-Q (2015) J Am Chem Soc 137:13228–13231
46. Vecchietti J, Collins SE, Delgado J, Małecka M, del Río E, Chen X, Bernal S, Bonivardi AL (2011) Top Catal 54:201
47. Han CW, Majumdar P, Marinero EE, Aguilar-Tapia A, Zanella R, Greeley J, Ortalan V (2015) Nano Lett 15(12):8141–8147
48. Reyes-Esqueda A, Bautista-Salvador A, Zanella R (2008) J Nanosci Nanotechnol 8:3843
49. Binet C, Badri A, Lavalley L-C (1994) J Phys Chem 98:6392–6398
50. Binet C, Daturi M, Lavalley J-C (1999) Catal Today 50:207–225
51. Collins SE, Cies JM, del Rio E, Lopez-Haro M, Trasobares S, Calvino JJ, Pintado JM, Bernal S (2007) J Phys Chem C 111:14371–14379
52. Cíes JM, el Río E, López-Haro M, Delgado JJ, Blanco G, Collins SE, Calvino J, Bernal S (2010) Angew Chem Int Ed 49:9744
53. Tabakova T, Boccuzzi F, Manzoli M, Sobczak JW, Idakiev V, Andreeva D (2006) Appl Catal A 298:127–143
54. Boccuzzi F, Chiorino A, Tsubota S, Haruta M (1996) J Phys Chem 100:3625–3631
55. Chen M, Goodman DW (2006) Acc Chem Res 39:739–746
56. Chen M, Goodman DW (2004) Science 306:252
57. Yoon B, Haakkinen H, Landman U, Worz AS, Antonietti JM, Abbet S, Juadai K, Heiz U (2005) Science 307:403–407
58. Worz AS, Heiz U, Cinquini F, Pacchioni G (2005) J Phys Chem B 109:18418–18426
59. Fielicke A, von Helden G, Meijer G, Simard B, Rayner DM (2005) J Phys Chem B 109:23935–23940
60. Alexeev O, Gates BC (1998) J Catal 176:310
61. Lyons KJ, Xie J, Mitchell WJ, Weinberg WH (1995) Surf Sci 325:85
62. Marinova TS, Chakarov DV (1989) Surf Sci 217:65
63. Kisters G, Chen JG, Lehwald S, Ibach H (1991) Surf Sci 245:65
64. Solymosi F, Novak E, Molnar A (1990) J Phys Chem 94:7250
65. Guerra CR, Schulman JH (1967) Surf Sci 7:229–249
66. Churchill MR, Li Y-J, Shapley JR, Foose DS, Uchiyama WS (1986) J Organometall Chem 312(1):121–131
67. Gelin IP, Coudurier G, Ben Y, Taarit C, Naccache C (1981) J Catal 70:32–40
68. Mihaylov M, Ivanova E, Thibault-Starzyk F, Daturi M, Dimitrov L, Hadjiivanov K (2006) J Phys Chem B 110:10383
69. Bourane A, Nawdali M, Bianchi D (2002) J Phys Chem B 106:2665
70. del Río E, Collins SE, Aguirre A, Chen X, Delgado JJ, Calvino JJ, Bernal S (2014) J Catal 316:210
71. Green IX, Tang W, Neurock M, Yates JT (2011) Science 333:736
72. Green IX, Tang W, McEntee M, Neurock M, Yates JT (2012) J Am Chem Soc 134:12717